In situ diffraction of highly dispersed supported platinum nanoparticles

Support-subtracted synchrotron diffraction patterns

39x19mm (300 x 300 DPI)

In situ diffraction of highly dispersed supported platinum nanoparticles

James R. Gallagher,[a] Tao Li,[b] Haiyan Zhao,[b] Jingjing Liu,[c] Yu Lei,[d] Xiaoyi Zhang,[b] Yang Ren,[b] Jeffrey W. Elam,[d] Randall J. Meyer,[c] Randall E. Winans,[b] and Jeffrey T. Miller *[a]

[a] Chemical Science and Engineering Division, Argonne National Laboratory, 9700 S Cass Ave., Argonne, IL, 60439 (USA)

[b] X-Ray Science Division, Advanced Photon Source, Argonne National Laboratory, 9700 S Cass Ave., Argonne, IL, 60439 (USA)

[c] Department of Chemical Engineering University of Illinois at Chicago 810 S. Clinton St. , Chicago, IL, 60607 (USA)

[d] Energy Systems Division, Argonne National Laboratory, 9700 S Cass Ave., Argonne, IL, 60439 (USA)

[*]Corresponding author: millerjt@anl.gov

1

Abstract

Highly dispersed supported metal nanoparticles are essential materials in the field of heterogeneous catalysis. For metallic nanoparticles (< 2 nm), structural information is rarely generated using conventional X-ray diffraction (XRD) owing to the extremely broad peaks in the diffraction pattern. The difficulty in detection is compounded by the partial oxidation of the nanoparticles on exposure to air during the measurement. Here we report how *in situ* synchrotron XRD provides structural information on reduced 1-2 nm Pt nanoparticles, which are unobservable by XRD when measured in air. Furthermore, for larger metal particles (> 2 nm) where diffraction patterns of the metallic phase are obtainable in air, we show that on exposure to air the surface is oxidized with a metallic core producing misleading results with respect to particle size and lattice parameter. Results from XRD are cross-correlated with scanning transmission electron microscopy and three other synchrotron X-ray techniques, small angle diffraction (SAXS), pair distribution function (PDF) and X-ray absorption spectroscopy (XAS), to provide detailed characterization of the structure of very small nanoparticles in the metallic phase.

Introduction

Supported noble metal nanoparticles are widely used heterogeneous catalysts in a large number of applications. To maximise catalytic performance and reduce the loading of the expensive noble metals, there is a strong desire to produce catalysts with the optimum catalytic activity per unit cost which typically translates into synthesizing catalysts with very high dispersions, corresponding to particle sizes close to 1 nm in diameter [1]. Important characteristics commonly determined for supported nanoparticle catalysts are the identity and composition of the active and inactive phases, the particle size distribution, bond distances, oxidation states, and how these change under reaction conditions. Experimental techniques used to define these properties include X-ray absorption spectroscopy (XAS)[2], pair distribution function (PDF)[3], small angle X-ray scattering (SAXS)[4], X-ray photoelectron spectroscopy (XPS)[5] and scanning transmission electron microscopy (STEM)[6]. XAS is conducive to *in situ* studies and has become a vital tool to characterize oxidation states, bond lengths and coordination numbers most often adjacent to the scattering atom. PDF provides similar structural information to XAS, but generally at slightly longer distances up to about 10 Å. Both methods provide local structural details, but averaged over all atoms making analysis of multiphase systems difficult. High-resolution STEM has developed significantly over the last 20 years allowing imaging of catalysts to sub-nanometer levels although it still suffers from a lack of structural detail. Furthermore, the vast majority of microscopes require high vacuum, which limits the ability to measure catalysts under realistic reaction conditions. XPS is a surface sensitive technique, which can provide the fraction of atoms in different oxidation states, although many spectrometers are unable to pre-treat samples or perform measurements under reaction conditions. SAXS can provide particle morphology and size distributions, overcoming the limited sampling statistics of STEM but yields little information about the catalyst phase assemblage, structure, or oxidation states.

XRD is the primary characterization tool in many fields of chemistry and materials science; however, the full capability is rarely exploited in heterogeneous catalysis due to the small particle size of the active phase and often the low metal loadings. It is

predominantly used *ex situ* to characterize supports or catalysts before or after reduction by comparing the measured data with reference patterns from a database while fitting the data using more advanced analysis techniques is less common. Such fitting can provide quantitative information on multiphase systems such as phase fractions and structure in addition to microstructural features such as size, strain and defect density which are valuable parameters to determine in order to further catalytic understanding[7-9]. XRD of very small (< 5 nm), supported nanoparticles is challenging predominantly due to the extremely broad peaks that are produced due to the insufficient number of lattice planes to effectively cancel incoherent scattering at angles close to the Bragg angle [4, 10]. The lack of diffraction peaks from metallic phases is sometimes used as evidence that the nanoparticles must be very small or amorphous [11]. However, numerical simulations have shown that Bragg diffraction peaks from Pt metal should be visible even for Pt clusters containing as few as 13 atoms, or ~0.6 nm in size [12]. The presence of diffraction peaks from the support overlapping with the peaks from the active phase can also hinder the detection and subsequent extraction of information from the pattern.

The purpose of the present study was to determine under what conditions 1-2 nm supported Pt nanoparticles with narrow and well-characterized size distributions could be analysed by conventional Bragg diffraction. We have chosen Pt/Al_2O_3 as our test system since supported Pt nanoparticles are one of the most widely studied heterogeneous catalysts due to their high catalytic activity for a number of catalytic transformations such as CO oxidation [13, 14], NO reduction [15, 16], hydrocarbon hydrogenation [17, 18], hydrogenolysis [19, 20] and naphtha reforming [21, 22]. Moreover, the high atomic number of Pt increases the scattering intensity. The structural investigation of such small metallic nanoparticles is vital to understanding their catalytic behaviour and XRD studies can provide useful information without the need for more exotic techniques. Herein we report how small, pre-reduced nanoparticles (1.5 nm) in the presence of air are almost fully oxidized and thus produce no metallic peaks in the diffraction pattern while larger particles (> 1.5 nm) are only surface oxidized thus peaks are observed from the metallic core. After reduction and *in situ* measurement under H_2, the small nanoparticles are

observed and the larger nanoparticles increase in size due to reduction of the surface oxide.

Experimental

Sample preparation

Supported platinum nanoparticles were prepared by atomic layer deposition (ALD). All the Pt samples were prepared in a continuous-flow stainless steel reactor operated under a base pressure of ~ 1 Torr [23]. Two types of supports were used, namely spherical alumina nanopowder (NanoDur™ mixture of delta and gamma Al_2O_3, average particle size ~40 nm, Alfa-Aesar) and multi-walled carbon nanotubes (CNTs, O.D. 10-20 nm, length 10-30 μm, pore volume = 4 ml/g, Cheap Tube Inc.). Prior to ALD, the CNTs were activated by refluxing in conc. HNO_3, 70 vol%, for 10 h at 120 °C while stirring. The mixture was filtered and washed with deionized water eight times, followed by drying at 80 °C for 8 h. Al_2O_3 was used as-received. The supports, Al_2O_3 (500 mg) and CNTs (200 mg) were evenly spread into separated flat stainless steel trays and loaded into the ALD reactor. Pt ALD was performed using trimethyl (methylcyclopentadienyl) platinum (IV) ($Pt(MeCp)Me_3$, Sigma-Aldrich) and oxygen at 250 °C [24]. Three samples were prepared using 2 and 5 Pt ALD cycles over Al_2O_3 and 2 cycles over CNTs, marked as $2cPt-Al_2O_3$, $5cPt-Al_2O_3$ and 2cPt-CNT, respectively. After synthesis all three samples were reduced in 3.5 % H_2 at 250 °C for 1 h before cooling to room temperature in He and then exposed to air for measurements.

Scanning transmission electron microscopy

Scanning Transmission Electron Microscopy (STEM) imaging was performed on pre-reduced catalysts using an aberration-corrected, cold-field emission gun microscope, JEOL JEM-ARM200CF, and operated at a primary energy of 200 keV. For high-angle annular dark-field imaging (HAADF), a spatial resolution of better than 70 pm can be achieved. In this work, HAADF images were used to determine the particle size

5

distribution. The particle sizes were analyzed using the software Comptage de particule (V2). Approximately particles from each sample were randomly chosen and counted for the particle size distribution plots.

Small-angle X-ray scattering

Small-angle X-ray scattering (SAXS) measurements were performed at the 12-ID-B beamline at the Advanced Photon Source (APS), Argonne National Laboratory (ANL). Data was acquired in transmission using X-rays at 14 keV (λ = 0.8856 Å) and a Pilatus 2M detector (Dectris Ltd.) with typical exposure times of 0.1-1.0 s. Samples were pressed into wafers and held inside a Linkam stage for measurement in air at room temperature. The 2-D scattering images were integrated to 1-D scattering intensity data using the Fit2D software [25] to yield plots of scattered intensity $I(Q)$ versus Q, where $Q = 4\pi (\sin\theta) / \lambda$. The data was fitted using Irena software [26]. Contributions from the support were subtracted to yield plots only containing information from the Pt particles.

Pair distribution function

In situ scattering data from pair distribution function (PDF) were collected at beamline 11-ID-B at the APS at ANL. High energy X-rays (58 keV, λ = 0.2127Å) were used in combination with a large amorphous silicon-based area detector. Samples were loaded in a Kapton capillary in a flow reactor [27] which allowed flow of reactant gas through the sample bed during the *in situ* PDF measurements [28]. A flow of 3.5 % H_2/He was introduced and the temperature was ramped to 250 °C, holding for 10 min. The catalysts were then cooled in 3.5 % H_2/He and the proper data for PDF was collected. The corresponding support was pretreated with the same procedure and the reference PDFs were taken at the same conditions. The 2-D scattering images were reduced to 1-D scattering intensity data using the Fit2D software [25]. The structure function S(Q) was obtained within software PDFgetX2 [29]. Direct Fourier transform of the reduced structure function F(Q) = Q[S(Q)-1] led to the reduced pair distribution function G(r) with Q_{max}= 20 Å^{-1}. Contributions from the supports were subtracted to yield differential PDF (d-

PDF). The d-PDFs show contributions only from the supported Pt species. Precise particle size was obtained from modelling the d-PDF data for the Pt nanoparticles after reduction, using PDFgui [29] by applying a face-center cubic (FCC) Pt structure with spherical shape.

X-ray absorption spectroscopy

X-ray absorption measurements (XAS) were acquired at the 10-BM beamline of the Materials Research Collaborative Access Team (MRCAT) at the APS, ANL. Data was acquired in transmission at the Pt L_3-edge (11.564 keV) in step-scan mode using ionization chambers optimized for the maximum current with linear response (~10^{10} photons detected/sec) with 10 % absorption in the incident ion chamber and 70 % absorption in the transmission X-ray detector. A Pt foil spectrum was acquired simultaneously with each sample measurement for energy calibration. Catalyst samples were pressed into a cylindrical sample holder consisting of six wells, forming a self-supporting wafer which was then placed in a quartz tube (1–in. OD, 10–in. length) sealed with Kapton windows by two Ultra-Torr fittings through which gas could be flowed. Measurements were first taken in air at room temperature on the pre-reduced catalysts before a flow of 3.5 % H_2/He was introduced and the samples reduced at 250 °C. The catalysts were then cooled in 3.5 % H_2/He and measurements performed at room temperature.

The normalized, energy–calibrated absorption spectra were obtained using standard methods and standard data reduction techniques were employed to fit the data using the WINXAS 3.1 software. Linear combination fitting was used to estimate the fraction of Pt metal and PtO present in the samples measured in air, in each case using the appropriate fully reduced catalyst as the Pt metal reference and an oxidized Pt nanoparticle as the reference for PtO. Experimental phase shift and backscattering amplitudes were measured using standard compounds of known structure, Pt foil (12 Pt-Pt at 2.77 Å) and $Na_2Pt(OH)_6$ (6 Pt-O at 2.05 Å). The EXAFS parameters were obtained by a least square

fit in *R*-space of the k^2-weighted Fourier Transform (FT) data. The Debye-Waller factor $\Delta\sigma^2$ was held constant at 0.002 for all fits.

X-ray diffraction

In situ XRD measurements were performed at the 11-ID-D beamline at the APS, ANL. Data was acquired in transmission using X-rays at 16 keV ($\lambda = 0.765334$ Å) and a Pilatus 2M detector with typical exposure times of 5-10 s. Samples were pressed into wafers and held inside a Linkam stage for *in situ* measurement under non ambient atmosphere and temperature. Measurements were first taken in air at room temperature on the pre-reduced catalysts before a flow of 3.5 % H_2/He was introduced and the temperature was ramped to 250 °C, holding for 10 min. The catalysts were then cooled in 3.5 % H_2/He and measurements performed at room temperature. The corresponding supports were treated with the same procedure and the reference measurements taken at the same conditions. The 2-D scattering images were integrated to 1-D scattering intensity data using the Fit2D software [25] to yield plots of scattered intensity versus *2θ*. The Le Bail method [30] was used to fit whole XRD patterns between 10° and 56° 2θ by means of Materials Analysis Using Diffraction (MAUD), a Java based refinement software [31]. MAUD treats each parameter associated with line broadening separately and thus can be used to deconvolute the contributions from the instrument and from the microstructural features of the sample which broaden the diffraction peaks. The instrumental contribution to the observed peak shape was determined using a standard (CeO_2, NIST SRM 674b) by refinement of the Cagliotti parameters which were then fixed for subsequent refinements of the catalyst samples. In addition to background polynomial, the following parameters were refined for each sample: lattice parameters, isotropic *Delf* particle size and isotropic microstrain [32, 33]. For 2cPt-Al_2O_3 measured in H_2, the microstrain was fixed from the corresponding value for 5cPt-Al_2O_3 as the refinement would not reach a stable minimum. Prior to Le Bail refinement, the background scattering from the supports were subtracted from the diffraction patterns from the catalysts using the PANalytical High Score Plus software. Where the support subtraction was not perfect, small regions were excluded from the refinement procedure.

Results

To obtain materials containing metal nanoparticles with nearly uniform size, atomic layer deposition (ALD) was used to deposit Pt on spherical Al_2O_3 nanopowder and carbon nanotube (CNT) supports. The average particle size of the Pt particles on Al_2O_3 was varied by adjusting the number of Pt ALD cycles (2 and 5 cycles). A single sample was prepared on the CNT support using 2 Pt ALD cycles. The Pt loading was determined by inductively coupled plasma (ICP) and yielded Pt loadings of 2.82 %, 15.1 % and 9.82 % for 2cPt-Al_2O_3, 2cPt-CNT and 5cPt-Al_2O_3 respectively. The higher Pt loading for the 2cPt-CNT compared to the 2cPt-Al_2O_3 results from the much higher specific surface area of the CNT.

In order to characterize the Pt particle size distributions after reduction and subsequent exposure to air, both STEM and SAXS measurements were performed. STEM micrographs are shown in Figure 1 and the SAXS data is shown in Figure 2. The imaging indicated a nearly spherical morphology for the Pt nanoparticles on all three samples and therefore the diameters of individual Pt particles were used to define the Pt particle size for each sample. The particle size increased with the number of Pt ALD cycles, but was relatively insensitive to the nature of the support, with average sizes for the 2cPt-Al_2O_3, 2cPt-CNT and 5cPt-Al_2O_3 of 1.2 ($\pm$0.3) nm, 1.5 ($\pm$0.3) nm and 1.9 ($\pm$0.5) nm, respectively. The raw SAXS data after support subtraction is shown in Figure 2a and the particle size distributions were calculated using a log-normal model assuming spherical nanoparticles as shown in Figure 2b. The data was fitted using a model with median particle diameters of 1.5 nm, 1.7 nm and 2.4 nm for the 2cPt-Al_2O_3, 2cPt-CNT and 5cPt-Al_2O_3 respectively. The standard deviation for all samples was around 0.4 nm. The trend in particle size is in good agreement with the STEM measurements although it should be noted that STEM measures number distributions whereas SAXS measures the volume weighted distribution. Despite this difference, the results from both methods indicate that the samples span a range of average particle sizes, and each sample has a narrow size distribution. For clarity, in the following discussions the samples will be referred to by the average particle size as measured by SAXS (i.e. 1.5, 1.7 and 2.4 nm).
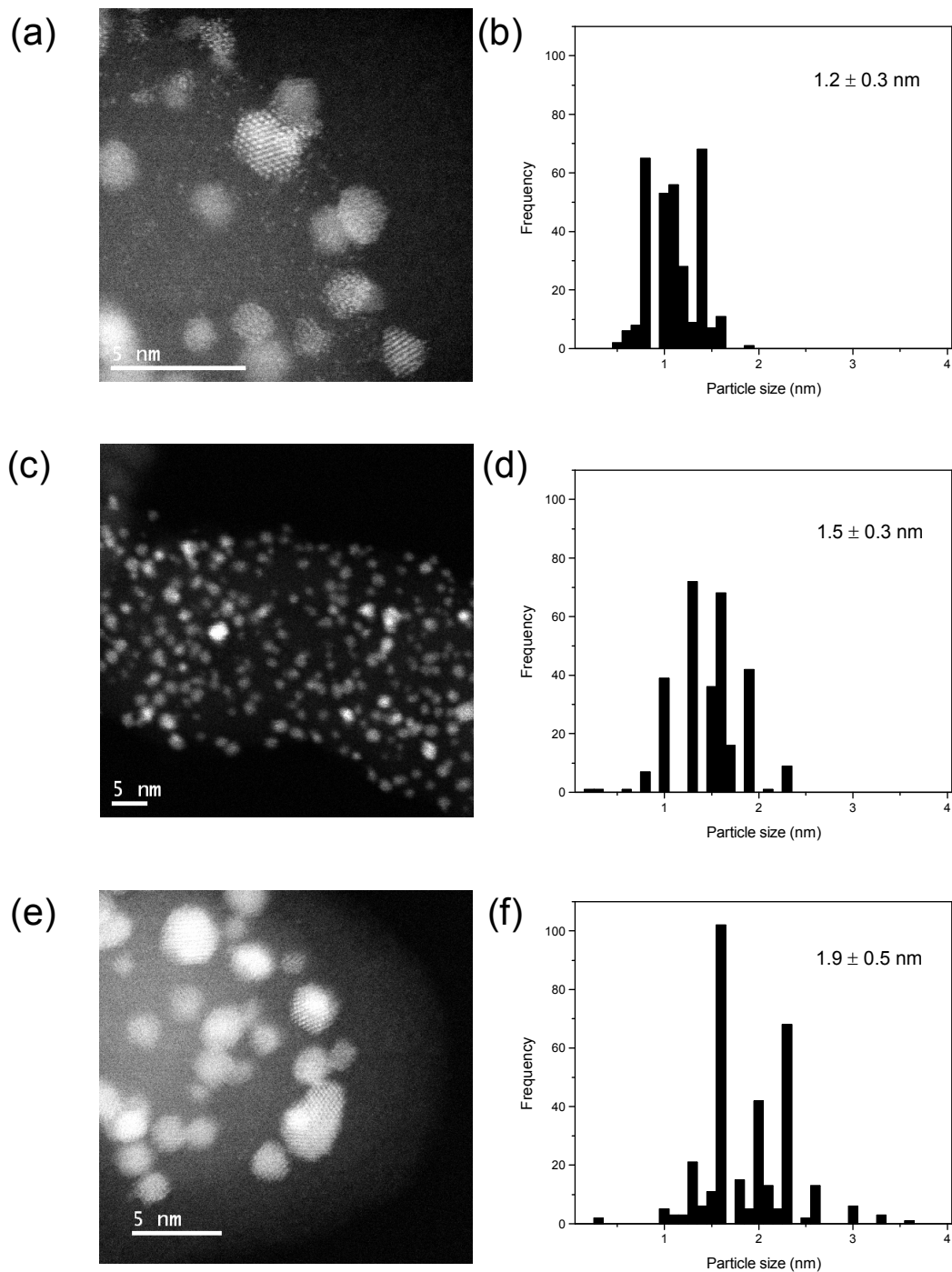
Figure 1. TEM micrographs and the corresponding particle size (number) distributions with mean and associated error ($\pm$ 1σ) of (a), (b): 2cPt-Al$_2$O$_3$, (b), (c): 2cPt-CNT and (d), (e): 5cPt-Al$_2$O$_3$.

The PDF analysis was carried out for all three samples in H_2 after reduction. The differential PDF data (d-PDF) in the range 1 to 20 Å is shown in Figure 3 and the refined parameters obtained from modelling are shown in Table 1. In the d-PDF plots, the position of the oscillation peaks directly gives the bond distance or interatomic distances in the structure [34]. Multiple oscillations (N >10) were observed in the d-PDFs, indicating that both local and intermediate range atomic structural information are included. The Pt-Pt bond distances were identified as 2.74, 2.76 and 2.77 Å for 2cPt-Al_2O_3, 2cPt-CNT and 5cPt-Al_2O_3 respectively. These values indicate a slight contraction in bond length from bulk Pt metal and are consistent with the trend obtained from EXAFS, discussed later. A great deal of structural information including lattice parameters, particle size and atomic displacement parameters are obtained by modelling the d-PDFs within PDFgui using a FCC Pt structure with spherical shape. The calculated d-PDFs shown in Figure 3 are well aligned with the experimental d-PDFs, which suggest the Pt nanoparticles are fully reduced with a crystalline FCC structure. The number of shells of atoms observed decreased with particle size and the values derived from the fitted model are in agreement with the trends from all other techniques. The particle sizes determined for 2cPt-AlO, 2cPt-CNT and 5cPt-AlO were 1.3, 1.6 and 2.1 nm respectively, following the same trend as the bond contraction independent of modelling. Meanwhile, the lattice parameters were also resolved from the fitting procedure yielding results consistent with the trend identified from XRD, discussed later.

(a)   (b)
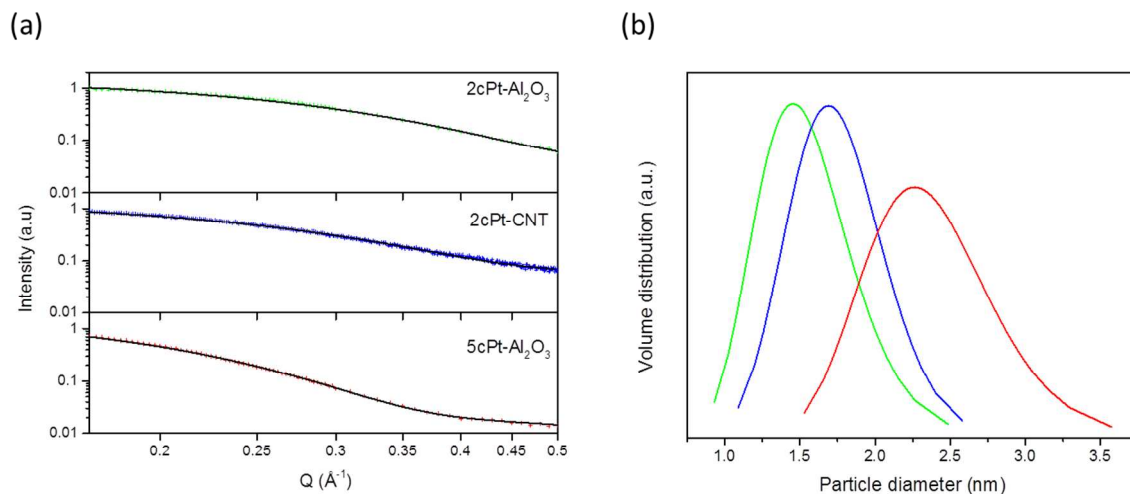
Figure 2. SAXS data for 2cPt-Al$_2$O$_3$ (green), 2cPt-CNT (blue) and 5cPt-Al$_2$O$_3$ (red) showing (a) raw data after support subtraction with calculated model in black and (b) the resulting particle size (volume) distributions.
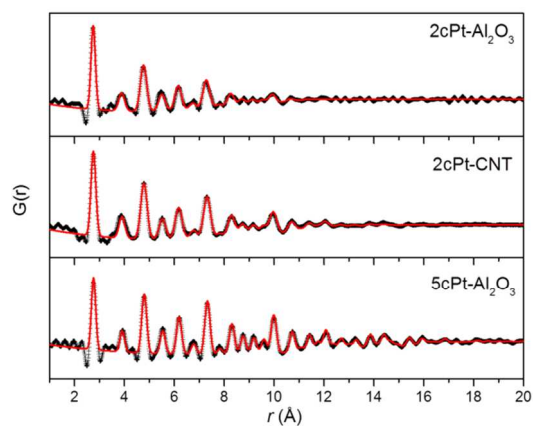
Figure 3. d-PDF plots after subtraction of the support contributions showing experimental data (black crosses) and calculated model (solid red line).

Table 1. Results from fitting of PDF data. Quoted errors are estimates based on the standard uncertainty in the scattering intensities and should be considered as lower bounds.

Sample	Phase	Lattice parameter, a (Å)	Particle size (nm)	ADP / $Å^2$	Bond distance (Å)	Shells
2cPt-Al$_2$O$_3$(H$_2$)	Pt	3.8999 (79)	1.3	0.009622	2.74	13
2cPt-CNT (H$_2$)	Pt	3.9130 (02)	1.6	0.010880	2.76	14
5cPt-Al$_2$O$_3$(H$_2$)	Pt	3.9200 (03)	2.1	0.005899	2.77	25

To interrogate the oxidation state of the samples, XANES spectra were measured on the pre-reduced catalysts in air and after reduction without exposure to air (Figures S1-S3). After reduction followed by exposure to air the XANES spectra were consistent with partial oxidation of Pt metal to PtO. To calculate the fraction of PtO to Pt metal, linear combination fitting of the XANES region of the spectra was performed. This analysis indicated that the degree to which oxidation occurred was dependent on the size of the nanoparticles with the Pt in 2cPt-Al$_2$O$_3$ being present as 97 % PtO whereas the 2cPt-CNT and 5cPt-Al$_2$O$_3$ showed 79 % and 67 % PtO, respectively. In other words, the PtO fraction decreased with increasing particle size. When measured in H$_2$ the XANES spectra for all three samples were consistent with full reduction to Pt metal by comparison with the Pt foil.

EXAFS spectra measured in air and under H$_2$ are shown in Figure 4 and the fitted parameters are detailed in Table 2 while the fits are shown in Figures S4-S9. The EXAFS measurements taken in air were substantially different from those in H$_2$ with all three samples containing peaks at approximately 1.6 Å (phase uncorrected) indicative of Pt-O scattering. The Pt-O bond distances were 2.05-2.06 Å, which is close to previously reported distances from DFT calculations [35]. This is consistent with partial oxidation of

13

the Pt nanoparticles as seen in the XANES region of the spectra which showed that particles of 1.5 nm were almost fully oxidized in air at room temperature. The Pt-O coordination numbers close to 4 which provides further evidence that the oxidized Pt species is PtO since many Pt(II) compounds are four-coordinate [36]. The 2.4 nm particles were also highly oxidized (67 % Pt(II) oxide). Compared to the fully reduced samples measured in H_2, the peaks at 2.4-2.9 Å due to Pt-Pt scattering were much lower in intensity. On exposure to air, a fraction of the metal was oxidized, lowering the amount of metallic Pt in the sample and therefore the number of Pt atoms in the metallic phase able to contribute to Pt-Pt scattering. The Pt-Pt scattering for 1.5 nm particles is very small; while a clear peak can still be identified for $5cPt-Al_2O_3$ which has 2.4 nm Pt particles. The measurements in H_2 showed only scattering from Pt-Pt interactions for all three samples and, therefore, were indicative of metallic Pt in agreement with the XANES results. The lower intensity relative to the Pt foil indicates a lower coordination number which is due to the increasing fraction of coordinatively unsaturated surface atoms as the particle size decreases. The fitted coordination numbers, Table 1, indicate a similar trend to the SAXS, STEM and PDF values for average particle size with $2cPt-Al_2O_3$ having the fewest nearest neighbors and $5cPt-Al_2O_3$ having the most. The Pt-Pt bond lengths of all three samples were slightly contracted by 0.01-0.02 Å relative to the foil, consistent with the trend from PDF. This phenomenon has been previously observed for small metallic nanoparticles [37, 38]. Since the measurements were performed in H_2, the relatively small contraction in bond length relative to previous studies [39] could be due to adsorbed H_2 causing bond relaxation [40].

(a)

(b)
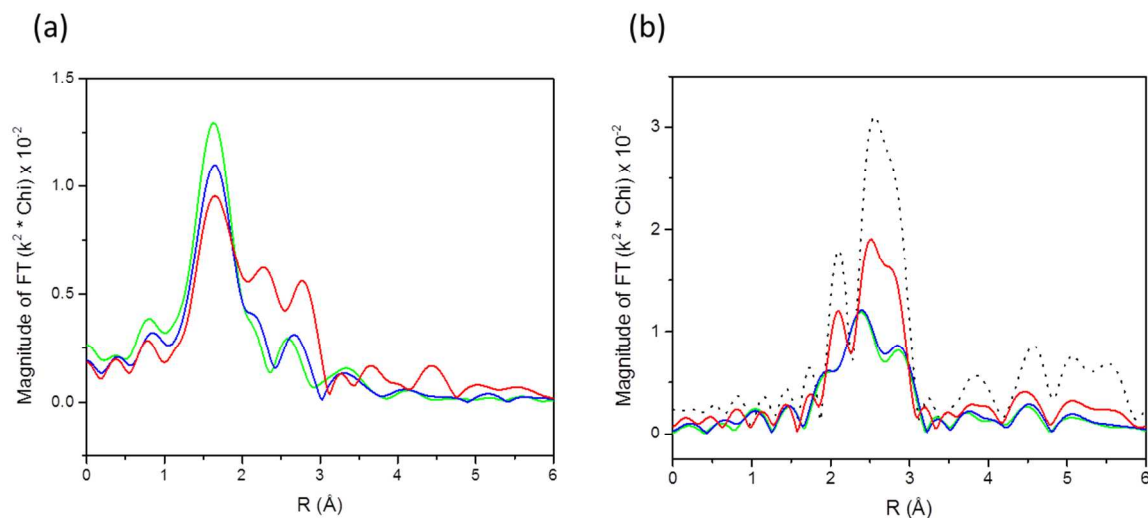
Figure 4. Pt L_3-edge magnitude of the FT of the EXAFS of 2cPt-Al$_2$O$_3$ (green), 2cPt-CNT (blue) and 5cPt-Al$_2$O$_3$ (red) measured in (a) air and (b) H$_2$. Pt foil is shown for reference (black, dashed). k^2: $\Delta k = 3.0\text{-}11.4$ Å^{-1}.

Table 2. Fitted EXAFS data of the samples measured in air and in H$_2$ at the Pt L-edge. N = coordination number; R = bond distance; $\Delta\sigma^2$ Debye-Waller factor; E_0 = energy offset.

Sample	Scattering pair	N	R (Å)	$\Delta\sigma^2$	E_0 (eV)
Na$_2$Pt(OH)$_6$ (ref)	Pt-O	6.0	2.05	0.000	0.00
Pt foil (ref)	Pt-Pt	12.0	2.77	0.000	0.00
2cPt-Al$_2$O$_3$ (air)	Pt-O	3.4	2.05	0.002	2.83
2cPt-Al$_2$O$_3$ (air)	Pt-Pt	1.6	2.59	0.002	-17.10
2cPt-CNT (air)	Pt-O	3.0	2.06	0.002	2.92
2cPt-CNT (air)	Pt-Pt	2.0	2.65	0.002	-11.76
5cPt-Al$_2$O$_3$ (air)	Pt-O	2.7	2.06	0.002	4.22

5cPt-Al$_2$O$_3$ (air)	Pt-Pt	4.1	2.72	0.002	-4.22
2cPt-Al$_2$O$_3$ (H$_2$)	Pt-Pt	7.7	2.75	0.002	-3.54
2cPt-CNT (H$_2$)	Pt-Pt	8.2	2.75	0.002	-2.26
5cPt-Al$_2$O$_3$ (H$_2$)	Pt-Pt	10.9	2.76	0.002	-2.16

The XRD patterns of the bare Al$_2$O$_3$ support in air and 2cPt-Al$_2$O$_3$ in air and H$_2$ are shown in Figure 5, illustrating that the diffraction patterns of 2cPt-Al$_2$O$_3$ were dominated by peaks arising from the Al$_2$O$_3$ support. The difficulty in detecting peaks from Pt is due to the low loading and high dispersion giving rise to extremely broad, low intensity diffraction peaks which can easily be overlooked if only visual inspection of a powder pattern is performed. For this reason, a direct analysis of the Pt phase was not possible without further data processing. The most comprehensive way to analyze diffraction peaks arising from two separate phases is to account for both phases using two structural models in the fitting procedure. Whilst it was possible to identify the support as predominantly δ-Al$_2$O$_3$, it was not possible to fit a suitable structural model that adequately accounted for all the support peaks due to the poorly understood nature of the structure of transition aluminas [41, 42]. Instead, in order to isolate the diffraction features arising from the Pt particles, the acquired diffraction pattern from the bare support was subtracted from the patterns of the Pt loaded catalysts and the resulting diffraction patterns are shown in Figure 6. Some parts of the subtracted diffraction patterns contained glitches where the subtraction of the support was non-perfect (see for example $2\theta = 22°$ and $32°$). This could be due to small changes in the Al$_2$O$_3$ support structure which could lead to shifts in the intensities or peak positions. Alternatively this could be due to changes in the absorption of the sample when loaded with Pt as compared to bare Al$_2$O$_3$ which could cause small variations in the peak intensities. In the fitting of the XRD data, discussed later, such clear glitch regions were excluded from the refinement;

16

however since there were still large regions of the diffraction patterns without such glitches, calculated profiles could still be satisfactorily fit.

When the pre-reduced $2cPt-Al_2O_3$ sample with SAXS particle size of 1.5 nm was measured in air, no diffraction peaks arising from Pt metal could be identified. However, broad diffraction peaks that were severely shifted from Pt metal positions were present, suggesting that they arose from a different phase, likely to be PtO. Even though PtO was the majority phase as determined by XANES, the diffraction pattern arising from this phase was weak suggesting a highly disordered structure. For 2cPt-CNT and $5cPt-Al_2O_3$, with SAXS particle sizes of 1.7 nm and 2.4 nm respectively, clear diffraction peaks belonging to FCC Pt metal were observed when the pre-reduced samples were measured in air. However, both diffraction patterns also contained features likely to be from PtO which were severely overlapped with the metal peaks. The diffraction pattern from the 1.7 nm particles more closely resembled that of the 1.5 nm particles with the broadened peak at *ca* 19° and the lower intensity of the higher angle peaks, suggesting a greater contribution from PtO. The 2.4 nm particles contained a small feature likely to be from PtO which manifests as a low-angle shoulder to the Pt metal peak at *ca* 19°. Conversely, when reduced and measured in H_2, without exposure to air, despite the noise due to imperfect support subtraction, clear diffraction peaks which could be indexed to Pt metal were observed for the 1.5 nm particles, thus indicating that even particles of such small size can be identified by XRD using careful background subtraction and analysis. Furthermore, the peaks of the 1.7 nm and 2.4 nm particles became narrower and no features from PtO could be observed following reduction in H_2.
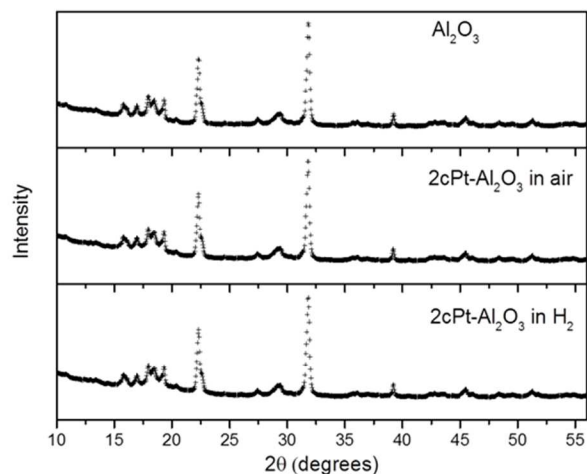
Figure 5. XRD plots of bare Al_2O_3 support (top) and 2cPt-Al_2O_3 in air (middle) and in H_2 (bottom). Plots are offset for clarity.

Subtraction of the support contribution from the diffraction patterns of the Pt loaded samples allowed the peaks arising from metallic Pt to be fitted using Le Bail refinement which uses an iterative least squares method to fit a calculated diffraction pattern to the observed data. Peak positions are constrained by the inputted unit cell while lattice and microstructural parameters such as particle size are refined to produce the best fit to the observed data points. The software which was used (MAUD) allows separation of instrumental and sample contributions to the diffraction peak broadening by measurement of a standard which possesses little microstructural broadening permitting all the broadening to be attributed to instrumental factors. When the sample of interest is then measured, any additional broadening can be attributed to microstructural features such as particle size and microstrain. The results of the refinements are shown in Table 3 and the plots showing the refined calculated fits are shown in Figures S10-S13. From the XRD measurements in air it was not possible to extract any quantitative structural information from the 1.5 nm or 1.7 nm particles due to the lack of Pt metal peaks in the former case and the interference of the PtO phase with the Pt metal phase in the latter case preventing a satisfactory refinement of the Pt metal structure. Hence, when measured in air the only sample where it was possible to calculate a Pt metal particle size was 5cPt-Al_2O_3 which

yielded a value of 2.4 nm. When the measurement was performed under H_2, the particle size increased to 3.3 nm. Both 2cPt-Al_2O_3 and 2cPt-CNT contained smaller Pt metal particles than 5cPt-Al_2O_3 when measured in H_2 with values of 1.4 nm and 2.6 nm respectively. The general trend is in agreement with the particle size measurements from all other techniques.

The lattice parameter extracted from the refinement of pre-reduced 5cPt-Al_2O_3 in air was approximately 0.02 Å larger than expected for bulk Pt (3.9236 Å) [43]. However, when measured in H_2 without exposure to air the lattice parameter decreased to a value approximately 0.03 Å smaller than the bulk. The lattice parameters for 2cPt-Al_2O_3 and 2cPt-CNT were also smaller than bulk, consistent with the trend identified from PDF measurements. The Pt-Pt bond distances calculated from the lattice parameters were 2.75 Å, 2.75 Å and 2.76 Å for 2cPt-Al_2O_3, 2cPt-CNT and 5cPt-Al_2O_3 respectively which are within error of the measurements from EXAFS. The refinements on the samples measured under H_2 also yielded a high degree of microstrain. This is related to there being a distribution of atom positions present which leads to a broadening of the diffraction peaks in addition to the broadening arising from the effect of particle size. As suggested by Polesz *et al.* a more rigorous method of accounting for the variation in atomic position due to surface strains may be to consider the nanoparticles as a two phase system [44]. Rapid appearance of diffraction peaks for 2cPt-Al_2O_3 were observed just 2 minutes after H_2 was introduced to the sample indicating that reduction of the surface oxide layer was facile (Figure S14). For 2cPt-CNT and 5cPt-Al_2O_3, the diffraction patterns also changed at low temperature with the peaks sharpening and increasing in intensity indicating that the size of the metallic core had increased to almost the final value after several minutes at low temperature (< 40 °C).
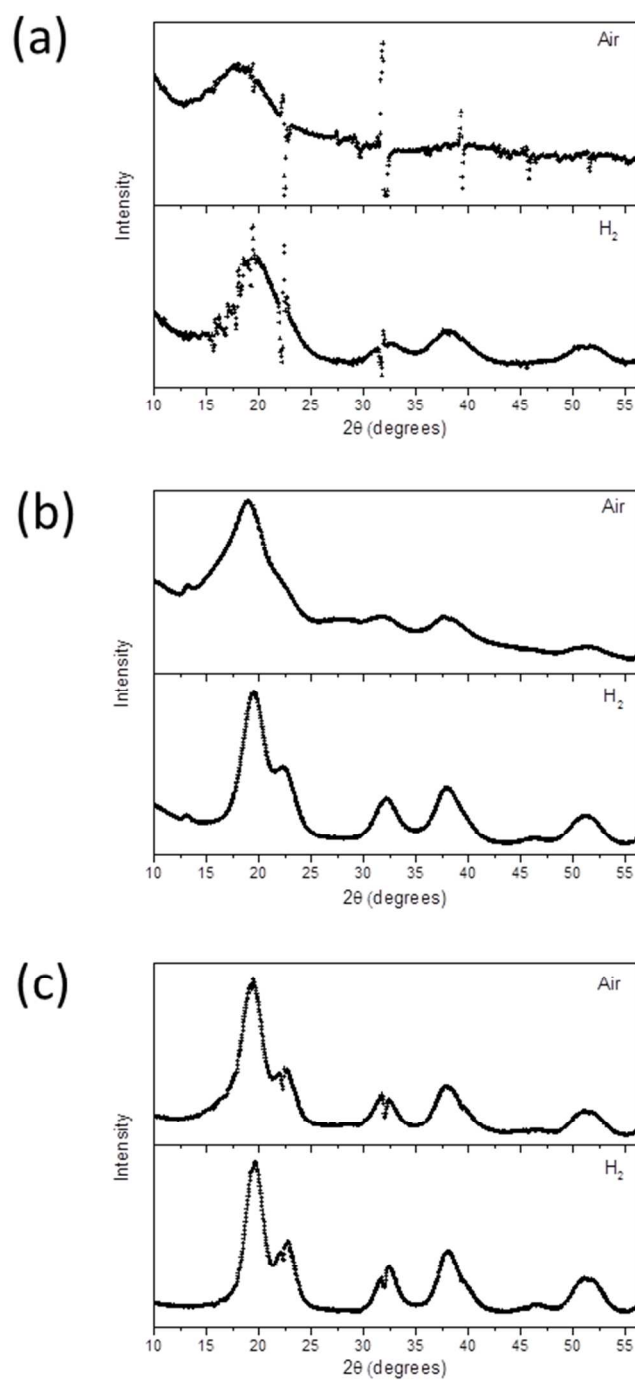
Figure 6. XRD plots after subtraction of the support in air (top) and in H_2 (bottom) of (a) 2cPt-Al_2O_3 and (b) 2cPt-CNT and (c) 5cPt-Al_2O_3.

Table 3. Results from Le Bail refinement of XRD data. Quoted errors are estimates based on the standard uncertainty in the powder diffraction pattern intensities and should be considered as lower bounds. *Fixed from refinement of 5cPt-Al$_2$O$_3$.

Sample	Phases detected	Lattice parameter, a (Å)	Crystallite diameter (nm)	RMS microstrain $<\varepsilon^2>^{1/2}$
2cPt-Al$_2$O$_3$ (air)	PtO	-	-	-
2cPt-CNT (air)	PtO + Pt	-	-	-
5cPt-Al$_2$O$_3$ (air)	PtO + Pt	3.9355(09)	2.4	0.0126(09)
2cPt-Al$_2$O$_3$ (H$_2$)	Pt	3.8833(19)	1.4	0.0137*
2cPt-CNT (H$_2$)	Pt	3.8956(07)	2.6	0.0184(05)
5cPt-Al$_2$O$_3$ (H$_2$)	Pt	3.8997(04)	3.3	0.0137(04)

Discussion

Using STEM, SAXS and PDF measurements, three ALD Pt samples were all found to have narrow particle size distributions, but different average particle sizes depending on the support and number of Pt ALD cycles performed. Although all of the techniques used in this study yielded slightly different absolute numbers for the average particle size, the general trend in all cases was the same and support the finding that the sample with the smallest Pt particles, 2cPt-Al$_2$O$_3$ has an average Pt particle size of 1.2-1.5 nm.

XANES and EXAFS measurements indicated that on exposure to air the metallic Pt particles were partially oxidized and the fraction of metallic Pt was dependent on the size

of the nanoparticles. For 2cPt-Al$_2$O$_3$, where the average particle size by SAXS was 1.5 nm, the Pt nanoparticles almost completely oxidized in the presence of air, with only 3 % metallic Pt and no measureable diffraction peaks due to Pt metal. The lack of measurable Pt diffraction peaks is likely for two reasons. First, the amount of Pt metal present was simply too low to be detected and second, oxidation was to such an extent that the decreased size of the remaining metallic cores produced diffraction peaks that were too broad to be distinguished from the background. Such surface oxides on Pt nanoparticles have been observed by XRD previously [45-47]. A different result was obtained for 5cPt-Al$_2$O$_3$, which contained 33 % metallic Pt in air, in that diffraction peaks that could be indexed to FCC Pt metal were observed. Compared to 2cPt-Al$_2$O$_3$, there was a much greater fraction of metallic Pt which aided detection in addition to the larger size of the metallic cores (2.4 nm from XRD) which produce narrower diffraction peaks. In the case of the 1.5 nm particles, the surface represents such a large fraction of the particles that almost the whole particle is oxidized leaving behind a very small metallic core.

When the diffraction pattern was collected in H$_2$, measurable diffraction peaks from Pt metal were observed for the 1.5 nm particles confirming that the absence of peaks in air was due to oxidation of the nanoparticles and not a lack of sensitivity for the measurement of small nanoparticles. The presence of peaks shows that it is possible to observe very small particles by XRD provided the measurement is taken under conditions where oxidation cannot occur, and careful background subtraction is performed. For the 2.4 nm particles, when measured in H$_2$, the average size of the metallic core increased by almost 40 %. This increase in the size of the metallic core is likely due to the reduction to Pt metal of surface oxides formed during exposure to air. Hence, measuring such particles in air leads to an underestimation of the Pt metal particle size. This discrepancy in the measured average particle size highlights the importance of measuring small nanoparticles under *in situ* conditions to correctly characterize the particle size. It is expected that as the average size of the particles increases the relative difference between measurement in air and H$_2$ will decrease as the surface becomes proportionally a smaller fraction of the whole particle. Hence, *ex situ* measurements in air of large particles are likely to be good approximations to the actual particle size.

In addition to the particle size, the lattice parameter of the Pt phase was also calculated and this capability provides further motivation for measurement under *in situ* conditions. The lattice parameter calculated for the 2.4 nm particles in air was larger than bulk Pt and suggests that surface oxidation may cause disorder of the surface leading to an increase in the average (metallic) Pt-Pt bond distance and hence an increase in the size of the unit cell [48]. It is possible that the expanded lattice parameter results from the overlap of the peaks due to the PtO phase causing an apparent peak shift to lower angle. However, expanded Pt-Pt distances were observed previously in a STEM study by Du *et al* [49] in which the authors ascribed to surface bonds to oxygen or sub-surface oxide which had diffused into the particle. This expanded Pt-Pt distance is at first in apparent contrast to the literature which suggests that interatomic distances are smaller in nanoparticles than in bulk due to the increased surface tension and lower coordination of the surface atoms as the surface:volume ratio increases [50-52]. However, this contradiction is reconciled by the results which showed that the lattice parameters were in fact smaller than bulk when the measurements were performed in H_2, and the particles were fully reduced. This trend of a contraction in the Pt-Pt bond distance is consistent with the EXAFS and PDF data and although the absolute changes in bond length are slightly different they are within the 0.02 Å error from EXAFS. The bond contractions are in the range previously reported for measurements performed in H_2.

The broad and low intensity diffraction peaks arising from the Pt metal nanoparticles made them difficult to detect, even when the measurements were performed in H_2 and without subtraction of the scattering from the support, their presence would have gone unnoticed. This outcome would have been even more likely had a laboratory diffractometer been used for the measurements as the signal to noise ratio would have been much lower. The high flux X-rays provided by a synchrotron insertion device beamline gave Pt peaks that were sufficiently intense to be resolved from the background noise without prohibitively long collection times. Moreover, the rapid collection times available at modern synchrotrons allow temporal resolution of seconds or less.

Even with the use of synchrotron radiation, the analysis of such broad peaks is still challenging. The significant overlap between Pt peaks makes unconstrained fitting of single peaks problematic and hence precluded implementation of the most frequently used method for determination of particle size from XRD patterns, the Scherrer equation which calculates the particle size based on the width of a single diffraction peak [53]. While lattice parameters can be calculated from a single diffraction peak for cubic materials, the accuracy is low and better results are obtained when calculating lattice parameters from several diffraction peaks. Additionally, use of the software MAUD for this analysis has the advantage of separating the contribution to the peak width from instrumental factors from the broadening effects due to the sample and in this way allows the particle size to be calculated more accurately. Without adequately accounting for the instrumental effects, underestimation of particle size will occur.

The analytical approach taken here should be generally applicable to other supported metal nanoparticle systems. Support crystallinity is likely to be a key factor in the ease with which diffraction peaks from small metal nanoparticles can be differentiated from the support. Supports such as SiO_2 – commonly used in heterogeneous catalysis - could be problematic since their poorly defined diffraction patterns make separation of support scattering from nanoparticle scattering more difficult. Supports which are typically more crystalline such as TiO_2 would likely be more amenable to analysis due to the large difference in peak width compared to the metal nanoparticles. Anomalous diffraction, which utilizes the modulation in atomic scattering factor close to the absorption edge to separate contributions from the nanoparticles and the support, has proven useful in previous studies[55, 56].

Conclusions

Highly dispersed Pt nanoparticles have been synthesized with narrow distributions over a range of average particle sizes to investigate the conditions under which Bragg diffraction can be performed on small nanoparticles. This work has shown that in order to collect useful XRD data on very small (< 2 nm) metallic nanoparticles deposited on supports,

measurements must be performed under a reducing atmosphere. For measurements performed in air, the metallic nanoparticles were oxidized to such an extent that the remaining metallic core was too small and at too low a concentration to produce measurable diffraction peaks. For larger nanoparticles (> 2 nm), the metallic core remaining after exposure to air was large enough for diffraction peaks to be observed but the structural parameters extracted from the data were different from those obtained under H_2. The measured particle size was smaller in air due to the oxidized surface and the derived lattice parameter was larger than bulk likely due to surface disorder from oxidation. Due to the low loadings and extremely broad nature of the diffraction peaks, even under H_2, high flux synchrotron radiation is required for detection. The rapid acquisition times (5-10 s) for such measurements mean that *in situ* time resolved monitoring of very small metallic nanoparticles is possible.

Acknowledgments

References

1. B. C. Gates, *Chem. Rev.*, 1995, 95, 511-522.
2. D. C. Koningsberger and D. E. Ramaker, in *Handbook of Heterogeneous Catalysis*, 2008, ch. 3, pp. 774–803.
3. K. W. Chapman and P. J. Chupas, in *In-situ Characterization of Heterogeneous Catalysts*, ed. J. C. H. a. P. J. C. J. A. Rodriguez J.A, John Wiley & Sons, Inc., Hoboken, NJ, USA, 2013.
4. M. Che and J. C. Vedrine, *Characterization of Solid Materials and Heterogeneous Catalysts: From Structure to Surface Reactivity*, Wiley, 2013.
5. W. Delgass, *Spectroscopy in Heterogeneous Catalysis*, Elsevier Science, 2012.

6.   P. L. Gai and E. D. Boyes, *Electron Microscopy in Heterogeneous Catalysis*, Taylor & Francis, 2010.
7.   T. Ungar and J. Gubicza, *Z. Kristall.*, 2007, 222, 114-128.
8.   R. Schlogl, in *Advances in Catalysis, Vol 52*, eds. B. C. Gates and H. Knozinger, Elsevier Academic Press Inc, San Diego, 2009, vol. 52, pp. 273-338.
9.   R. P. Marin, S. A. Kondrat, J. R. Gallagher, D. I. Enache, P. Smith, P. Boldrin, T. E. Davies, J. K. Bartley, G. B. Combes, P. B. Williams, S. H. Taylor, J. B. Claridge, M. J. Rosseinsky and G. J. Hutchings, *ACS Catalysis*, 2013, 3, 764-772.
10.   A. Cervellino, C. Giannini, A. Guagliardi and M. Ladisa, *Phys. Rev. B*, 2005, 72.
11.   Y. Sun, L. Zhuang, J. Lu, X. Hong and P. Liu, *J. Am. Chem. Soc.*, 2007, 129, 15465-+.
12.   D. Bazin, L. Guczi and J. Lynch, *Appl. Catal. A-Gen.*, 2002, 226, 87-113.
13.   A. Golchet and J. M. White, *J. Catal.*, 1978, 53, 266-279.
14.   A. C. Chen and P. Holt-Hindle, *Chem. Rev.*, 2010, 110, 3767-3804.
15.   R. Burch, J. P. Breen and F. C. Meunier, *Appl. Catal. B-Environ.*, 2002, 39, 283-303.
16.   W. S. Epling, L. E. Campbell, A. Yezerets, N. W. Currier and J. E. Parks, *Catal. Rev.-Sci. Eng.*, 2004, 46, 163-245.
17.   S. D. Lin and M. A. Vannice, *J. Catal.*, 1993, 143, 539-553.
18.   N. R. Shiju and V. V. Guliants, *Appl. Catal. A-Gen.*, 2009, 356, 1-17.
19.   M. Vaarkamp, J. T. Miller, F. S. Modica and D. C. Koningsberger, *J. Catal.*, 1996, 163, 294-305.
20.   M. A. Dasari, P. P. Kiatsimkul, W. R. Sutterlin and G. J. Suppes, *Appl. Catal. A-Gen.*, 2005, 281, 225-231.
21.   R. Burch and L. C. Garla, *J. Catal.*, 1981, 71, 360-372.
22.   M. R. Rahimpour, M. Jafari and D. Iranshahi, *Appl. Energy*, 2013, 109, 79-93.
23.   J. W. Elam, M. D. Groner and S. M. George, *Rev. Sci. Instrum.*, 2002, 73, 2981-2987.
24.   T. Aaltonen, M. Ritala, T. Sajavaara, J. Keinonen and M. Leskela, *Chem. Mat.*, 2003, 15, 1924-1928.
25.   A. P. Hammersley, S. O. Svensson, M. Hanfland, A. N. Fitch and D. Hausermann, *High Pressure Res.*, 1996, 14, 235-248.
26.   J. Ilavsky and P. R. Jemian, *J. Appl. Crystallogr.*, 2009, 42, 347-353.
27.   P. J. Chupas, K. W. Chapman, C. Kurtz, J. C. Hanson, P. L. Lee and C. P. Grey, *J. Appl. Crystallogr.*, 2008, 41, 822-824.
28.   P. J. Chupas, M. F. Ciraolo, J. C. Hanson and C. P. Grey, *J. Am. Chem. Soc.*, 2001, 123, 1694-1702.
29.   C. L. Farrow, P. Juhas, J. W. Liu, D. Bryndin, E. S. Bozin, J. Bloch, T. Proffen and S. J. L. Billinge, *J. Phys.-Condes. Matter*, 2007, 19.
30.   A. Lebail, H. Duroy and J. L. Fourquet, *Mater. Res. Bull.*, 1988, 23, 447-452.
31.   L. Lutterotti, D. Chateigner, S. Ferrari and J. Ricote, *Thin Solid Films*, 2004, 450, 34-41.
32.   R. Delhez, T. H. Dekeijser and E. J. Mittemeijer, *Fresenius Zeitschrift Fur Analytische Chemie*, 1982, 312, 1-16.
33.   L. Lutterotti and P. Scardi, *J. Appl. Crystallogr.*, 1990, 23, 246-252.
34.   T. Egami and S. J. L. Billinge, *Underneath the Bragg Peaks: Structural Analysis of Complex Materials*, Pergamon, 2003.
35.   N. Seriani, Z. Jin, W. Pompe and L. C. Ciacchi, *Phys. Rev. B*, 2007, 76.
36.   R. L. DeKock and H. B. Gray, *Chemical Structure and Bonding*, University Science Books, 1989.
37.   J. T. Miller, A. J. Kropf, Y. Zha, J. R. Regalbuto, L. Delannoy, C. Louis, E. Bus and J. A. van Bokhoven, *J. Catal.*, 2006, 240, 222-234.
38.   H. Y. Zhao, T. M. Nenoff, G. Jennings, P. J. Chupas and K. W. Chapman, *J. Phys. Chem. Lett.*, 2011, 2, 2742-2746.
39.   Y. Lei, J. Jelic, L. C. Nitsche, R. Meyer and J. Miller, *Top. Catal.*, 2011, 54, 334-348.
40.   J. H. Kang, L. D. Menard, R. G. Nuzzo and A. I. Frenkel, *J. Am. Chem. Soc.*, 2006, 128, 12068-12069.
41.   I. Levin and D. Brandon, *J. Am. Ceram. Soc.*, 1998, 81, 1995-2012.
42.   Y. Rozita, R. Brydson, T. P. Comyn, A. J. Scott, C. Hammond, A. Brown, S. Chauruka, A. Hassanpour, N. P. Young, A. I. Kirkland, H. Sawada and R. I. Smith, *ChemCatChem*, 2013, 5, 2695-2706.
43.   J. W. Arblaster, *Platin. Met. Rev.*, 1997, 41, 12.

44. B. Palosz, E. Grzanka, S. Gierlotka, S. Stel'makh, R. Pielaszek, U. Bismayer, J. Neuefeind, H. P. Weber, T. Proffen, R. Von Dreele and W. Palosz, *Z. Kristall.*, 2002, 217, 497-509.
45. V. Gnutzmann and W. Vogel, *Z. Phys. D-Atoms Mol. Clusters*, 1989, 12, 597-600.
46. W. Vogel, *J. Phys. Chem. C*, 2008, 112, 13475-13482.
47. H. Imai, K. Izumi, M. Matsumoto, Y. Kubo, K. Kato and Y. Imai, *J. Am. Chem. Soc.*, 2009, 131, 6293-6300.
48. P. Rzeszotarski and Z. Kaszkur, *Phys. Chem. Chem. Phys.*, 2009, 11, 5416-5421.
49. K. Du, F. Emst, M. C. Pelsozy, J. Barthel and K. Tillmann, *Acta Mater.*, 2010, 58, 836-845.
50. C. Solliard and M. Flueli, *Surf. Sci.*, 1985, 156, 487-494.
51. R. Lamber, S. Wetjen and N. I. Jaeger, *Phys. Rev. B*, 1995, 51, 10968-10971.
52. Z. X. Huang, P. Thomson and S. L. Di, *J. Phys. Chem. Solids*, 2007, 68, 530-535.
53. P. Scherrer, *Gottingen Nachrichten* 1918, 2, 98.
54. J. I. Langford, *J. Appl. Crystallogr.*, 1978, 11, 10-14.
55. K. S. Liang, S. S. Laderman and J. H. Sinfelt, *J. Chem. Phys.*, 1987, 86, 2352-2355.
56. O. Ducreux, B. Rebours, J. Lynch, M. Roy-Auberger and D. Bazin, *Oil Gas Sci. Technol.*, 2009, 64, 49-62.
57. S. V. Tsybulya and D. A. Yatsenko, *J. Struct. Chem.*, 2012, 53, S150-S165.
58. P. Scardi, M. Leoni and K. R. Beyerlein, *Z. Kristall.*, 2011, 226, 924-933.
59. C. Kumpf, *Appl. Phys. A-Mater. Sci. Process.*, 2006, 85, 337-343.
60. T. Hyde, *Platin. Met. Rev.*, 2008, 52, 129-130.